Nano Research

Open Access

Research Article

Correlation between structure, microstructure and electrochemical properties of Prussian white cathode material for sodium-ion batteries

Nataliya Yu. Samoylova[1] ✉, Marina E. Donets[1], Roman N. Vasin[1], Sergei V. Sumnikov[1], Ekaterina A. Korneeva[1], Alexander S. Sohatsky[1], Evgeny V. Andreev[1], Svetlana G. Protasova[2], Rais N. Mozhchil[2], and Nickolay A. Kolyshkin[3]

[1] *Joint Institute for Nuclear Research, Dubna 141980, Russia*
[2] *Institute of Solid State Physics and Chernogolovka Scientific Research Center of Russian Academy of Sciences, Chernogolovka 142432, Russia*
[3] *National Research Center Kurchatov Institute, Moscow 123182, Russia*

Cite this article: *Nano Research*, **2025**, *18*, 94907280. https://doi.org/10.26599/NR.2025.94907280

ABSTRACT: Sodium hexacyanoferrate, or Prussian white (PW), is a cheap cathode material for rechargeable sodium-ion batteries, exhibiting high capacity and charge/discharge rate. Tailoring structure and microstructure of PW to further improve its properties, in particular, cycling stability, is an important task to achieve for successful commercial applications of sodium-ion batteries. Here, the relation of grain refinement and thermal treatment with crystal structure, structural phase transition sequences and electrochemical properties of the PW are studied. The ball-milling process and subsequent drying at high temperatures induce the transformation of the initial rhombohedral structure of the pristine commercial Prussian White powder into a multiphase compound of dehydrated rhombohedral and cubic structures with different average crystallite sizes. The increased surface area of the effectively milled cubic phase promotes its transition into the dehydrated rhombohedral Prussian White at temperatures below 100 °C. Electrodes based on the milled Prussian White powder demonstrate a capacity of ~ 110 mAh·g^{-1} (compared to ~ 80 mAh·g^{-1} for the non-milled commercial powder) at 10 C cycling rate and better cycling stability, retaining a larger part of their initial specific capacity after 300 charge/discharge cycles than those based on non-milled material. It is shown that high-spin and low-spin Fe redox processes in Prussian white-based electrodes are also affected by ball milling.

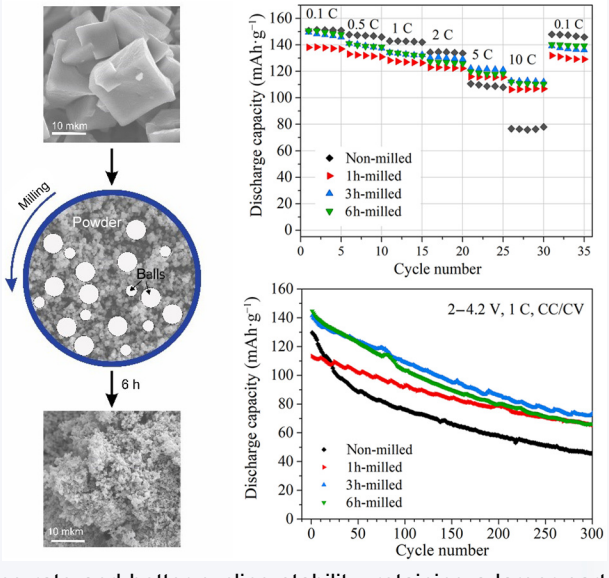

KEYWORDS: Prussian white, sodium-ion batteries, ball milling, phase transitions, X-ray diffraction

1 Introduction

The rapid development of lithium-ion technologies and the active use of lithium-ion batteries in different devices led to a sharp increase in the consumption of lithium, whose natural reserves are limited. The chemical current sources based on sodium ions are considered as alternative current sources [1]. Sodium is one of the most abundant elements in the Earth's crust, and it is close to lithium in terms of its chemical properties. The study of promising compounds for use as cathode materials for sodium-ion batteries (SIB) is highly relevant today [2–4].

Among these materials are Prussian blue analogues, particularly a sodium hexacyanoferrate, Prussian white (PW), with a general formula of $Na_{2-x}Fe[Fe(CN)_6]_{1-y}\cdot\square_y\cdot mH_2O$ (□—$Fe(CN)_6$ vacancies, *y*—their number). It is characterized by high capacity and charge/discharge rates [5–7]. Its open-frame structure can easily accommodate sodium ions and ensure their rapid transport. However, standard environmental methods for the PW synthesis suggest the presence of a number of $Fe(CN)_6$ vacancies and structural water in the initial material structure, which affects the

Received: November 9, 2024; **Revised:** January 22, 2025
Accepted: February 1, 2025

✉Address correspondence to rny03@nf.jinr.ru

stability of the crystal lattice during electrochemical cycling, leads to a capacity decrease after the long-term operation, and hinders the widespread commercialization of SIBs based on PW materials.

Currently, a number of studies are focused on developing conditions for removing the structural water from the hexacyanoferrates. It was shown, that the preheating of electrodes with commercial PW material leads to an increase in capacity; however, this could damage the material and lead to a rapid capacity decay after repeating charge/discharge processes [8, 9]. Moreover, the commercially available PW powder has low capacity at high cycling rates: ~ 68 mAh·g^{-1} at 560 mA·g^{-1} [8]. For the same PW material, most recently we have reported capacity values of 100 mAh·g^{-1} at 850 mA·g^{-1} and 83 mAh·g^{-1} at 1700 mA·g^{-1} achieved when using 15 wt.% content of carbon additive content in electrode composition [9].

Another possible way to improve the electrochemical performance of the PW material is to modify its microstructure. It is known that the electrochemical characteristics of the battery (e.g., specific capacity, power, charge/discharge rates, etc.) correlate with the structure and microstructure of the cathode material. In particular, current values can be increased by reducing the size of the active material particles composing the electrode. A smaller particle size means shorter diffusion paths of ions and a larger surface area of the active material being in contact with the conductive additives and electrolyte [10]. Particle size reduction via ball milling has been shown to improve electrochemical properties in different lithium-ion battery electrode materials [11–13]. But currently, there are only a few studies of the ball milling effect on the electrochemical properties of cathode materials for other battery types, e.g., hexacyanoferrates. Previously, it was shown that prolonged ball milling (up to 9 h) did not destroy the crystal structure of the copper hexacyanoferrate used in calcium-ion batteries and improved the charge/discharge capacity; however, after 200 cycles, the structural collapse of the electrode occurred [14]. Recently, it has been reported that the ball milling synthesis produces highly crystalline Prussian blue analogue $Na_{2-x}Mn[Fe(CN)_6]$ materials with a highly reversible sodium-ion storage behavior effect [15] and a capacity of 126.6 mAh·g^{-1} at a current density of 2000 mA·g^{-1} [16]. On the other hand, it was discovered that the mechanical milling leads to the formation of a completely amorphous or glassy state in several Prussian Blue analogues, e.g., $Fe^{III}[Fe^{II}(CN)_6]_{3/4}\cdot nH_2O$ (144 h milling), or $K_{0.32}Cu[Fe(CN)_6]_{0.63}\cdot nH_2O$ (2 h milling) [17].

Currently, phase transitions between PW crystalline phases during Na ion intercalation/deintercalation are widely investigated, and their relation to the electrode capacity is studied [18–20]. However, to our knowledge, there are no comprehensive studies of the ball milling effect on the crystal structure, microstructure, and electrochemical properties of the Prussian white.

In this work, we investigated the influence of ball milling on the structure and electrochemical properties of the commercial sodium hexacyanoferrate $Na_{1.8}Fe[Fe(CN)_6]\cdot 2.2H_2O$ cathode material using electron microscopy, X-ray diffraction (XRD), X-ray photoelectron and Fourier-transform infrared (FTIR) spectroscopy, gas absorption, and electrochemical methods.

2 Materials and method

Pristine commercial PW powder (Altris, Sweden) was ball milled (600 rpm) using a planetary ball mill with a 100-mL zirconia jar containing the PW material and zirconia balls with diameters of 5 and 10 mm. The mass ratio of sample-to-balls was 1:20. Acetone was added to the jar to make the milling process more homogeneous. The milling times were 1 h (further demoted as a "1h-milled" sample), 3 h ("3h-milled"), and 6 h ("6h-milled"). After the milling, the powders were dried for 24 h in a vacuum oven at 120 °C, except for a part of the 6 h-milled powder that was not dried ("6h-milled-nd"). The electrodes were prepared by coating an NMP based slurry consisting of the PW active material, Ketjenblack and polyvinylidene difluoride binder in a weight ratio of 70/15/15 onto graphitized aluminum foil. After the preparation, the electrodes were additionally dried at 120 °C for 24 h and stored in the argon-filled glovebox.

Scanning electron microscopy (SEM) measurements of the pristine and milled powders were performed at Hitachi S-3400 N microscope. For transmission electron microscopy (TEM) measurements, the milled powders were first ultrasonically dispersed in ethanol, and then the lightest fractions of the resulted suspensions, separated by a centrifuge, were deposited on a thin film of pure carbon supported by copper TEM grids. TEM analysis was performed at the Thermoscientific Talos F200i field emission transmission electron microscope operating at 200 kV.

The crystal structures of the materials were examined using powder XRD at the PANalytical Empyrean diffractometer using Cu-Kα radiation. For measurements at ambient conditions, all the powders were packed into a specially designed, sealed argon-filled cell to avoid contact with humid air during diffraction experiments. Additionally, the milled powders were measured by XRD *in situ* during heating from room temperature up to 250 °C with a 1 °C/min rate. The powders were placed into an open cuvette under vacuum; measurement time was 5 min per pattern, and the range of scattering angles was $2\theta = 10°–45°$.

The phase transformations of the materials were studied in *operando* X-ray diffraction experiments at the PANalytical Empyrean diffractometer and synchrotron diffraction at the STM station of the Kurchatov Synchrotron Radiation Source (NRC Kurchatov Institute, Moscow, Russia) at monochromatic radiation with a wavelength of 0.65297 Å. Before experiments, electrodes were preheated in vacuum at 180 °C for 12 h. A specialized XRD cell with a beryllium window was used for experiment at the PANalytical Empyrean diffractometer. It was assembled with the electrode based on the non-milled PW, 1 M $NaClO_4$ in ethylene carbonate/diethyl carbonate (EC/DEC, 1:1 v/v) solution with a 3 wt.% fluoroethylene carbonate (FEC) additive as an electrolyte, a glass fiber (Whatman GF/F) as a separator, and sodium as a counter electrode. For synchrotron *operando* experiment, the electrode based on the 3h-milled PW material was assembled in the coin cell with 2 mm Kapton-sealed window in the casing, using the same electrolyte, separator and counter electrode.

FTIR spectroscopy analysis was performed on a Nicolet iS20 spectrometer (Thermo Fisher Scientific) in attenuated total reflectance mode (Smart iTX, ZnSe single crystal) at room temperature. The wavenumber range was set to 4000–520 cm^{-1}, the scanning wavenumber resolution was 2 cm^{-1}, and the number of scans was 32.

X-ray photoelectron spectroscopy (XPS) measurements were carried out using a Thermo Fisher K-Alpha spectrometer with a monochromatic X-ray Al-Kα source (1486.6 eV). The powders were mounted onto a sample holder with 3M 665 double-sided adhesive tape. For surface charge compensation, an electron flood gun was used. The beam spot was 400 μm. Full survey XPS scans

were collected with a pass energy of 200 eV and a 0.5 eV step size. High-resolution scans of C 1s and Fe 2p were recorded with 20 eV pass energy and 0.05 eV step size, and there were no less than 50 scans for Fe 2p spectra. All data were analyzed with Shirley background and Gaussian–Lorentzian functions by CasaXPS (version 2.3.23PR1.0) software, where spectra were calibrated by C 1s = 284.8 eV. Preliminary XPS experiments were made at a Kratos AXIS Ultra DLD spectrometer with a Mg-Kα irradiation source ($h\nu$ = 1253.6 eV) with a resolution of 0.8 eV (Fig. S1 in the Electronic Supplementary Material (ESM)).

N_2 gas adsorption experiments were performed at 77 K using a Quantachrome NOVA 4200E instrument. Before the experiments, the samples (300–400 mg) were evacuated at 1 mbar residual pressure at 200 °C for 3 h. The surface area was calculated by the multi-point Brunauer–Emmett–Teller (BET) analysis method [21].

CR2032 coin-type cells were assembled with electrodes in an argon-filled glovebox using rolled-to-foil sodium as a counter electrode, and a glass fiber (Whatman GF/F) as a separator. Before cell assembly, the electrodes were preheated in a vacuum at 180 °C for 12 h. The electrolyte was 1 M $NaClO_4$ dissolved in an EC/DEC (1:1 v/v) solution with a 3 wt.% FEC additive. The mass of the active material was ≈ 9.2–10.4 mg. The first cycling program consisted of 5 sequential charge/discharge CC cycles at each of 7 rates (0.1, 0.5, 1, 2, 5, 10, and 0.1 C), according to the theoretical capacity of 170.8 mAh·g^{-1} of vacancy-free sodium hexacyanoferrate [5]. The second cycling program, so-called long cycling, consisted of the initial cycle at 0.1 C rate (CC cycle) and subsequent 300 cycles (CC/CV charging at 1 and 0.1 C, and CC discharging at 1 C). Both types of cycling were performed at room temperature between 2 and 4.2 V (vs. Na/Na^+) using the Neware battery testing system.

3 Results and discussion

3.1 Crystal structure, microstructure and valence state characterization

Let us review the microstructural features of the PW powders, as demonstrated by SEM images (Fig. 1). Pristine PW particles have a cube-like morphology with some growth defects and a characteristic particle size of ~ 20–50 μm (Fig. 1(a)). After 1 h of milling, initial particles are mostly destroyed to sub-μm powder, but some occasional larger particles of ~ 5 μm size are still visible (Fig. 1(b)). In 3h-milled powder, these larger particles become scarcer, and their size further decreases (Fig. 1(c)). In 6h-milled powder, practically all particles are < 1 μm size (Fig. 1(d)). TEM images show fragmentation of the 1h-, 3h-, and 6h-milled powders into particles with sizes of down to several hundred nm, ~ 100 nm, and several nm, respectively; however, larger particle fragments are also clearly visible (Fig. 1).

The specific surface area of the pristine and milled samples dried at 120 °C was determined from gas absorption experiments using BET analysis (see Fig. S2 in the ESM for nitrogen gas absorption isothermal curves and BET plots). The ball milling increases the surface area of the powder from 34.29 m^2·g^{-1} for the non-milled sample to 47.94 and 53.68 m^2·g^{-1} for the 3h- and 6h-milled samples, respectively. This relatively small change in the surface area after milling could result from the inhomogeneous fragmentation of pristine particles, the aggregation of smaller particles or the significant water loss due to heating of the milled powders.

Increasing the surface area enables the powder to absorb more water from the ambient air. To verify this assumption, the experiment on the powder hydration with water vapors has been performed: The PW powders were placed into the circular cases with a diameter of 2 cm and preheated at 180 °C for 3 h in vacuum, then immediately placed on the scales and weighed for 70–75 min during the water absorption process (see Fig. S3 in the ESM for a mass increment of the PW samples due to water absorption). Indeed, the amount of water absorbed in the first 70 min increases with milling time and is 5.9 mg for the non-milled powder and 10.3, 13, and 15.7 mg for the 1h-, 3h-, and 6h-milled powders, respectively.

Figure 2 shows the FTIR spectra of the initial PW powder and the milled samples. The water uptake by the powders during the milling process manifests itself when observing the region of FTIR spectra associated with υ(O–H) absorption bands at 3500–3700 cm^{-1} [22]. With increasing milling time, the υ(O–H) band at 3595 cm^{-1} notably increases in intensity (Fig. 2(b)). This agrees with the observation of Ojwang et al. [23] that an increase in relative

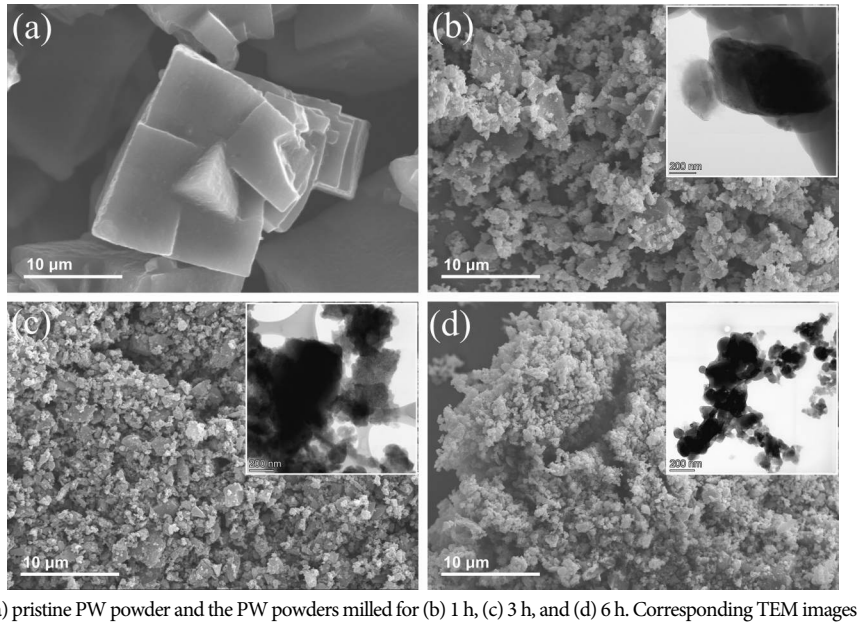

Figure 1 SEM images of the (a) pristine PW powder and the PW powders milled for (b) 1 h, (c) 3 h, and (d) 6 h. Corresponding TEM images are shown in insets.

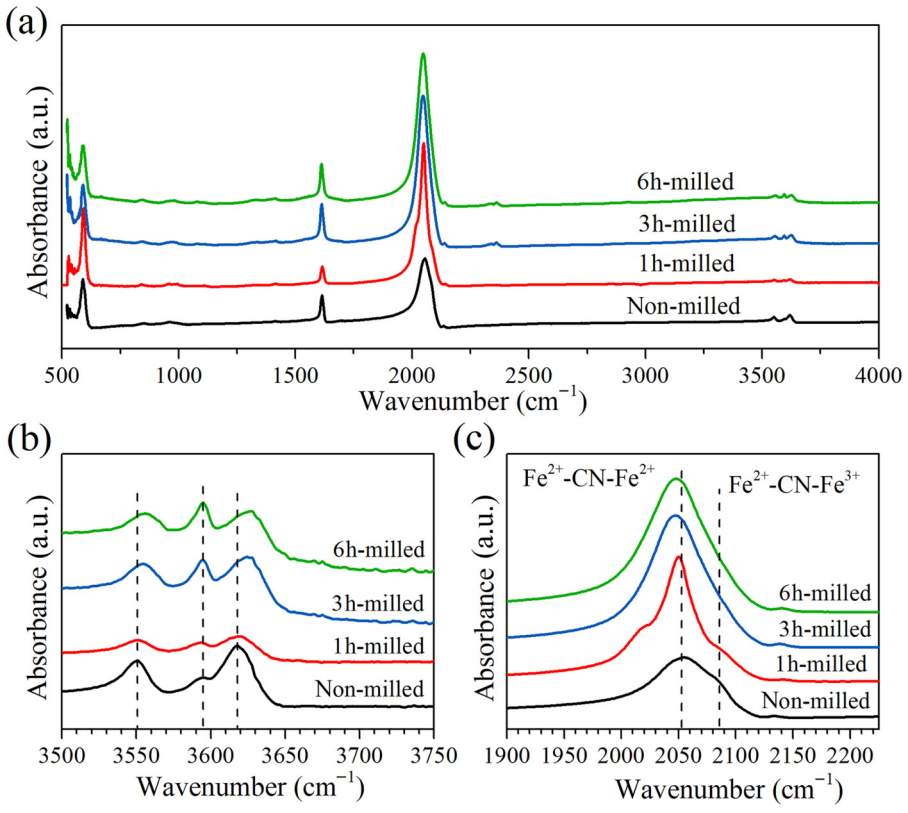

Figure 2 FTIR spectra of (a) non-milled and milled PW samples at room temperature and (b) and (c) selected regions of spectra with important absorption bands.

humidity from 0% up to 75% gives rise to an additional band between the initial two bands at 3551 and 3618 cm^{-1}. Moreover, two bands observed at 3551 and 3618 cm^{-1} for the non-milled sample are shifted to the higher wavenumbers in the spectra of the milled powders. This may indicate a decrease in the average oxidation state of iron cations in the whole system [22].

Analysis of the υ(C≡N) stretching vibration band at 2000–2100 cm^{-1} (Fig. 2(c)) was additionally used to characterize the electronic state of PW samples, since the cyanide bridge C≡N is extremely sensitive to the oxidation state of iron cations [22]. In the spectrum of non-milled powder, the observed maximum at around 2050 cm^{-1} and a shoulder at around 2085 cm^{-1} can be interpreted as the υ(C≡N) vibrations in Fe^{2+}–CN···Fe^{2+} and in Fe^{2+}–CN···Fe^{3+}, respectively [9]. Thus, υ(C≡N) vibration in Fe^{2+}–CN···Fe^{3+} indicates partial oxidation of its surface during long-term storage of the PW material, even in an argon atmosphere. In the IR spectra of the 1h- and 3h-milled samples, the υ(C≡N) vibration in Fe^{2+}–CN···Fe^{3+} decreases with increasing milling time, and disappears in the spectrum of the 6h-milled powder. Moreover, compared to the position at 2050 cm^{-1} in the FTIR spectrum of the non-milled sample, the υ(C≡N) band is shifted to lower wavenumbers in the spectra of the milled powders. This could be interpreted as a reduction of iron, according to [24]. Thus, the milling process breaks up the PW particles, exposing a non-oxidized surface and, therefore, decreasing the average oxidation state of an active surface.

For a more detailed analysis, the oxidation states of the initial and milled PW powders were further investigated by XPS. Peaks in the XPS spectra indicate the presence of Na, Fe, C, N, and O in the powders (Fig. 3(a)). The Fe 2p spectra (Fig. 3(b)) include two groups of Fe $2p_{1/2}$ and Fe $2p_{3/2}$ peaks. The Fe $2p_{3/2}$ regions were fitted with four components at ~ 708.6, ~ 710.2, ~ 712.5, and ~ 714–714.9 eV (satellite peak), associated with low-spin (LS) Fe^{2+}, high-spin (HS) Fe^{3+}, high-spin Fe^{2+} states, and most probably with iron oxide, respectively [25–27]. The quantitative analysis of the Fe $2p_{3/2}$ peaks (Figs. 3(c)–3(f)) has revealed higher content of HS-Fe^{3+} state and lower content of LS-Fe^{2+} in the non-milled sample compared to the milled powders (Fig. 3(g)). This observation agrees with the IR results on the decrease in the average oxidation of the powder surface after milling and the PW oxidation mechanism [23], when HS iron is oxidized first: $O_2 + 2H_2O + 4Na_2Fe^{2+}[Fe^{2+}(CN)_6] \rightarrow 4NaFe^{3+}[Fe^{2+}(CN)_6] + 4NaOH$.

In the milled samples, the fraction of the HS-Fe^{3+} state increases with milling time from 18.3% to 24.9% (Fig. 3(g)). Additional surface oxidation can occur due to contact with air during preparation for XPS measurement. Since the surface area of the milled powders increases with milling time (Fig. S2 in the ESM), oxidation will be more pronounced in samples milled for a longer time.

The 716–710 eV binding energy range could also be attributed to iron oxide multiplets [23]. Despite the fact that the XRD experiment has not revealed a substantial amount of ferrous or ferric-type oxides in the surface layer of ~ 10–20 μm (see below Section 3.2), they could be present on the surface of the powder particles and make a notable contribution to the XPS signal, which probes a depth of ~ 10 nm. Thus, the iron oxide contribution to the XPS spectrum cannot be completely excluded, and it could affect the analysis results and change the reported ratios of LS-Fe^{2+}, LS-Fe^{3+}, and HS-Fe^{2+} at different milling times (Fig. 3(g)).

XRD patterns of the pristine and milled PW powders are shown in Fig. 4. Patterns were processed with the MAUD software [28] utilizing the Rietveld method [29] to determine the phase composition of the powders, crystal structure parameters and

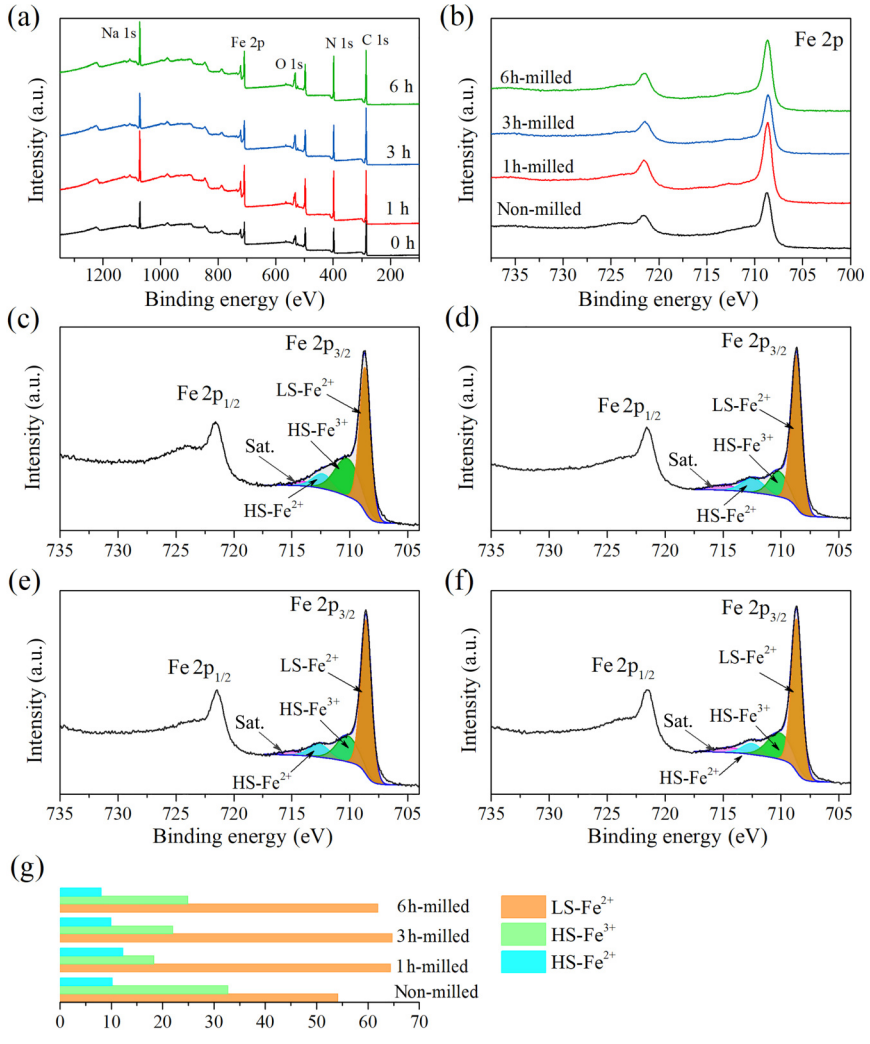

Figure 3 XPS spectra of the PW powders: (a) general view and (b) enlarged region with Fe 2p peaks. Fitting of Fe 2p XPS spectra regions for (c) the non-milled, (d) 1h-milled, (e) 3h-milled, and (f) 6h-milled PW powders. (g) Calculated content of LS-Fe^{2+}, HS-Fe^{3+}, and HS-Fe^{2+} states in the samples. Non-milled and milled PW samples at room temperature and ((b) and (c)) selected regions of spectra with important absorption bands.

microstructural characteristics. Diffraction peaks of the following crystalline PW phases were found in diffraction patterns and their crystal structures were taken from corresponding references: the dehydrated rhombohedral "d-R" phase (space group $R\bar{3}$) [18], the rhombohedral "R" (space group $R\bar{3}$) phase [19] and the cubic phase (space group $Fm\bar{3}m$) [30]. The refined XRD patterns and the obtained structural and microstructure parameters are given in Fig. S4 and Tables S1–S5 in the ESM.

The pristine PW powder was previously revealed to contain two crystalline PW phases: the main R phase and the subsidiary cubic phase, with volume fractions of 84 vol.% and 16 vol.%, respectively [9]. After drying at 120 °C, the non-milled sample is also in a two-phase state, containing 67.2 vol.% of R-phase and 28.8 vol.% of cubic phase (Fig. 4(c)). Both phases are well crystallized with refined average crystallite (i.e., coherently scattering domain) sizes over 2000 Å, which is about the resolution limit of the used X-ray diffraction setup. Additionally, a very weak diffraction peak of some impurities is present at a scattering angle of ~ 32.5°. It was argued that this peak is characteristic of the $Na_4[Fe(CN)_6]$ compound [8], which may be formed as a result of degradation of the PW [23]. Our recent results [9] suggest that the impurity may be a NaO_2 oxide with $Fm\bar{3}m$ space group and unit cell parameter $a \approx 5.51$ Å. Assuming that the impurity phase is NaO_2, its content in the pristine dried PW may be estimated as ~ 4 vol.%, and it decreases with the milling time increase (to ~ 2 vol.% after 6 h). Its unit cell parameter remains within a 5.5–5.52 Å interval.

In all PW powders, dried (Fig. 4(b)) and not dried (Fig. 4(a)), the R-phase disappears after the milling, and the cubic phase is retained. In the dried PW powders, all diffraction peaks of the cubic phase become asymmetric with longer "tails" towards higher scattering angles (Fig. 4(b)), which we interpret as the presence of the second cubic phase with a smaller unit cell parameter (by ~ 0.015–0.07 Å) and a smaller average crystallite (i.e., coherently scattering domain) size. In 6h-milled-nd powder, diffraction peaks are characterized by longer "tails" towards lower scattering angles (Fig. 4(a)); therefore, the second cubic phase in the not-dried powder should have a larger unit cell parameter. Consequently, the reported Rietveld refinement of milled powders diffraction patterns featured two cubic phases. The Rietveld refinement of XRD patterns of the milled PW powders, made using only one cubic phase, leads to substantially worse results (Fig. S5 in the ESM).

The average crystallite size in the first cubic phase remains at a

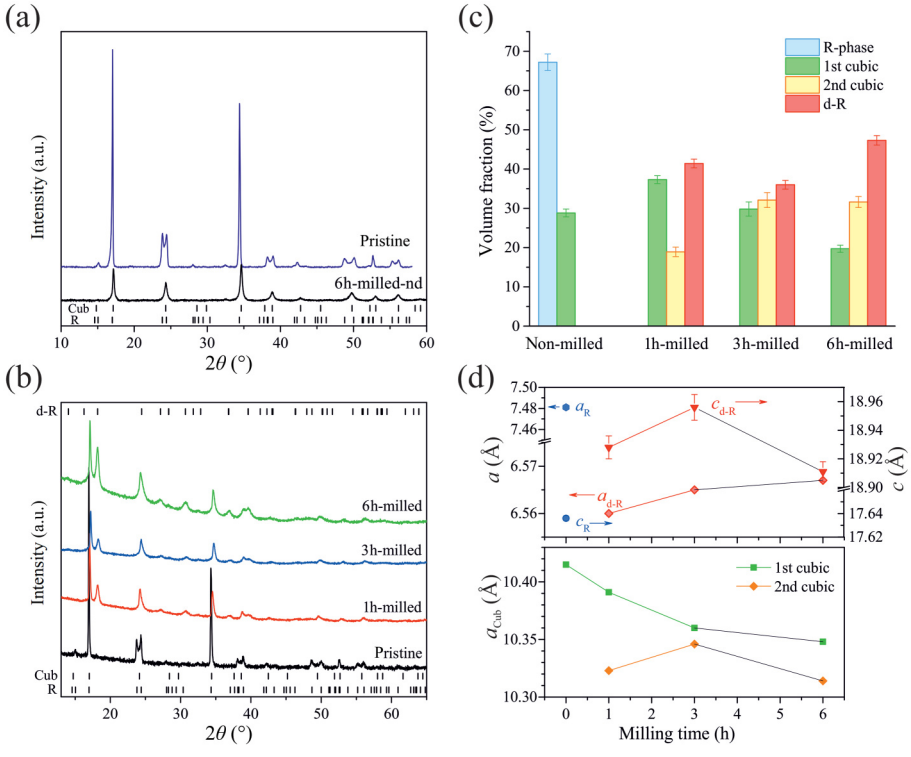

Figure 4 XRD patterns of (a) pristine and 6h-milled-nd PW powders, and (b) pristine and 1h-milled, 3h-milled, 6h-milled PW powders (after drying at 120 °C); vertical ticks indicate calculated diffraction peak positions for the cubic, d-R and R phases. (c) Volume fractions of the two cubic, d-R and R phases, and (d) their unit cell parameters for the dried PW powders.

level of > 1600 Å during milling, and the crystallites in the second phase are refined with longer milling time (469 Å after 1 h milling, 173 Å in dried, and 250 Å in not dried PW after 6 h milling). The unit cell parameter of the first cubic phase gradually decreases with the milling time in dried PW powders (Fig. 4(d)). The unit cell of the second phase does not demonstrate consistent behavior. It decreases to 10.323 Å after 1 h of milling, then increases after 3 h of milling, and further decreases to 10.314 Å after 6 h (Fig. 4(c)). In the 6h-milled-nd PW powder, the refined unit cell parameter value of the second cubic phase is 10.399 Å (vs. 10.374 Å for the first cubic phase). This value is comparable to the unit cell parameter of the cubic phase in pristine PW powder.

While only cubic phases are present in the 6h-milled-nd PW powder (where the second cubic phase is dominant with a volume content over 60%), in the dried powders, a dehydrated d-R phase appears. This phase normally forms in Na-based hexacyanoferrates upon heating to temperatures over ~ 100 °C [8, 9] (also see the next section). The d-R phase content is 41.4 vol.% in 1h-milled dried PW powder. In 3h-milled powder, it decreases to 36 vol.% and increases to 47.3 vol.% in 6h-milled powder. The content of the first cubic phase in dried PW powders gradually decreases with milling time, from 37.3 vol.% after 1 h of milling to 19.7 vol.% after 6 h of milling. The volume content of the second cubic phase in dried PW powders is the smallest after 1 h of milling: 18.9 vol.%. It increases to 32.1 vol.% after 3 h of milling and is practically unchanged after 6 h of milling. The unit cell parameter *c* of the d-R changes non-linearly with the milling time: It reaches the maximum value after 3 h of milling, and the minimum value of 18.911 Å is reached after 6 h of milling. The unit cell parameter *a* and the crystallite size of the d-R phase are practically independent of milling time, remaining at the levels of 5.56–5.57 and 340–350 Å, respectively.

Let us analyze the observed structural and microstructural peculiarities. The initial PW powder is in a two-phase state. The formation of the cubic phase is most likely related to the water captured from the ambient air (~ 40% humidity). It is known that increased humidity induces the transformation of rhombohedral and monoclinic hexacyanoferrate structures into the cubic phase [23, 31]. It was demonstrated that the commercial PW powder also transforms into cubic structures when stored in ambient air conditions for several weeks [9].

During milling, PW powders may additionally adsorb water from acetone, where the water could have been easily dissolved. Moreover, an increase in temperature during mechanical milling could also promote the transformation into the cubic phase. Consequently, the R-phase completely transforms. Two cubic PW phases are observed in all milled PW powders: dried and not dried. It was shown that a ball-milling process may indeed result in the separation of the initial material into two fractions, one of which is practically non-milled and the other one is more effectively milled (has a much smaller crystallite size compared to the first one) (e.g., [32]). Therefore, it is possible to assume that the second cubic phase in milled PW powders is more efficiently milled as its crystallite size decreases with the milling time, while the first cubic phase remains practically non-milled.

Comparing 6h-milled-nd and 6h-milled PW powders, we note that about half of both milled cubic phases transformed into the d-R phase. The unit cell parameters of both cubic phases decrease after drying, but the parameter of the effectively milled phase decreases more significantly. It was reported that there is no sodium loss in the PW structure due to thermal dehydration [31]. Therefore, this change in unit cell parameters may be attributed only to changes in water content. During milling, the more

effectively milled second cubic phase more effectively uptakes water, and its unit cell parameter increases. During pre-heating at 120 °C this phase is also more effectively dehydrated due to the increase in its surface area. But the non-linear dependence of the second phase volume fraction and unit cell parameter on milling time in dried PW powders indicates that the process of dehydration may be more complex.

Another interesting observation is that the d-R crystallite size seems independent of the milling time. It means that the limiting factor for the size is most likely the temperature and not the amount of water in the cubic phase. We note that the crystallite sizes given in Table S1 in the ESM are volume-weighted averages derived from diffraction peak breadths. Valuable microstructural information for understanding processes in milled PW powders, such as crystallite size distributions, might be derived from the analysis of diffraction peak profiles, but this procedure requires data measured with high resolution and much better counting statistics.

To conclude, in milled PW powders dried at 120 °C, a longer milling time resulted in an increased content of smaller cubic-phase particles, which more effectively adsorb water from the ambient medium. Both effectively milled and practically non-milled cubic-phase particles undergo the transition into the d-R phase during drying. The phase composition of the dried PW powders (Fig. 4(c)) is caused by a combination of the partial particle refinement during the milling process, water uptake into the different-sized particles of the initial R-phase during milling (causing their transition into the cubic structure), the efficiency of the water removal from the particles of the PW cubic phases by heating to 120 °C, and the dependence of cubic → d-R phase transition temperature and kinetics on all these factors.

3.2 Phase evolution during heating and cycling process

Depending on the synthesis procedure and sodium content of PW compounds, they can crystallize in monoclinic (space group $P2_1/n$) [18, 23, 31, 33, 34], hydrated rhombohedral R [35] or cubic [34, 36–39] structures. During heating, Na-based hexacyanoferrates, including commercial PW [8, 9], undergo a usual sequence of phase transitions, with the monoclinic phase (not observed in our experiments) transforming into the R-phase between 30 and 40 °C [40], which in turn transforms into the cubic phase, and finally to the dehydrated rhombohedral d-R phase under further heating [31, 40, 41]. Different temperatures of the transitions between these phases are reported in the literature for the different experimental techniques and reviewed in detail in our previous work [9].

Figure 5 shows the selected region of the XRD patterns map for non-milled and 6h-milled-nd PW powders measured during heating up to 250 °C in vacuum (10^{-2} mbar). Under the heating, the diffraction peaks 110 and 104 of the initial R phase of the non-milled PW powder are slowly merging into one, indicating the transition into the cubic phase that is completed at around 100 °C (Fig. 5(a)). The single cubic phase exists in a narrow temperature interval up to 113°C and then starts transforming into the dehydrated d-R phase: Its broad 012 diffraction peak appears in the diffraction patterns at ~ 18.1°.

During heating of the 6h-milled-nd powder, the initial cubic phase starts transforming into the d-R phase at ≈ 82 °C, then both phases coexist up to 175 °C (Fig. 5(b)) compared to 190 °C when heating the non-milled sample. As revealed in the gas absorption experiment (Fig. S2 in the ESM), the surface area of the PW powder increases due to milling process, which in turn leads to more effective powder dehydration during heating. As a result, the temperature of transition from the cubic into the d-R phase decreases, and the volume fraction of the formed d-R phase in the samples preheated at the same temperatures is expected to be larger in the milled PW powder. The similar effect was recently observed for the synthesized PW powder with a particle size of ~ 1 μm: Compared to commercial Na-enriched PW powder with a particle size of ~ 10 μm, the structural phase transitions under heating in vacuum were shifted to lower temperatures by ~ 10 °C [42].

Recently, phase transitions in the pristine commercial PW materials during their sodiation-desodiation under electrochemical cycling were thoroughly investigated using X-ray and neutron diffraction methods [9]. Reversible transformations between the hydrated rhombohedral R phase (in the discharged sodiated state), the dehydrated rhombohedral d-R phase, and the cubic phase (which is a single phase in a completely desodiated state) occur in a fresh PW material during charge–discharge. The presence of the rhombohedral R phase was found to depend on a level of electrode hydration: Preheating an electrode at different temperatures in a range of 140–200 °C reduces a volume fraction of this phase and reduces the voltage range of its existence proportionally to the preheating temperature [9]. Figure 6 shows the *operando* XRD patterns of the half-cells with the non-milled PW and 3h-milled PW materials as an active material measured during charge-discharge (for the non-milled PW, Fig. 6(a)) and during discharge (for the 3h-milled PW, Fig. 6(b)). For the both samples, transitions between the cubic, d-R and R phases occur during sodiation/desodiation. During the sodium intercalation into the

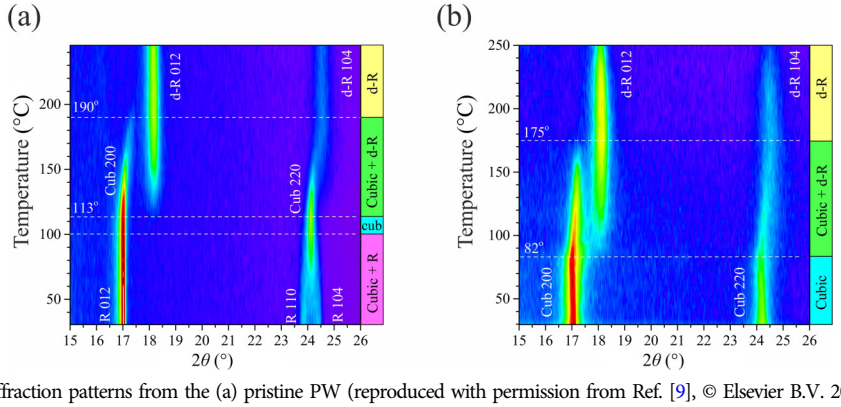

Figure 5 2D map of X-ray diffraction patterns from the (a) pristine PW (reproduced with permission from Ref. [9], © Elsevier B.V. 2024) and (b) 6h-milled-nd PW powders during heating up to 250 °C in vacuum. Miller indices mark individual diffraction peaks of rhombohedral (R), cubic (Cub), and dehydrated rhombohedral (d-R) phases. Color bars show the ranges of existence or co-existence of different structural phases.

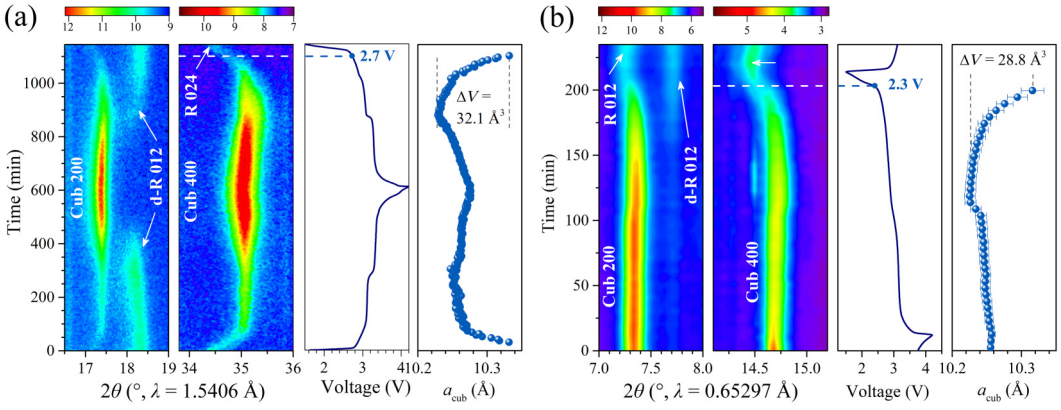

Figure 6 Fragment of 2D map plot of X-ray diffraction patterns of the electrodes (a) with non-milled PW material measured during charge/discharge at 0.1 C rate and (b) with 3h-milled PW material measured during discharge at 0.25 C rate.

material structure, the cubic cell in both materials undergoes quantitatively similar volume changes ΔV (32.1 and 28.8 Å^3 for the non-milled and 3h-milled materials, respectively), which is about 3%. The main difference in these two-phase transition sequences is in the voltage range of the R-phase appearance. During discharge, the phase transition from the cubic phase to the R-phase in the electrode based on milled PW begins at a lower voltage (2.3 V, Fig. 6(b)) compared to the electrode based on non-milled PW (2.7 V, Fig. 6(a)). Therefore, the observed impact of milling on the phase transition sequence is similar to the aforementioned effect of preheating temperature increasing, which is another proof of more efficient dehydration of the milled material at the stage of the electrode preheating compared to the original material.

3.3 Electrochemical properties

Figure 7 shows capacities of the PW-based electrodes with a weight composition ratio (PW/Ketjenblack/PVdF) of 70/15/15 at different rates of cycling in the 2–4.2 V voltage range. The starting discharge capacity of the electrode based on pristine PW powder charged at a 0.1 C rate is 151 mAh·g^{-1}, which is notably lower than the theoretical capacity value of 170.8 mAh·g^{-1}. Calendering the electrode with the same pristine PW as active material would increase the specific capacity to 160 mAh·g^{-1} [9]. However, it may be expected that different particle sizes of the active material would influence the inelastic deformation of the material during the calendering of the electrodes. Therefore, to exclude the calendering impact on the results, we studied the uncalendered electrodes.

The specific capacity of all electrodes decreases with increased charge/discharge rates because of the relatively slow sodium intercalation into the hexacyanoferrate structure. But the character of this reduction depends on the milling time. When the rate is increased from 0.1 C to 2 C, the specific capacity of the pristine PW decreases to 133.7 mAh·g^{-1} (89% of the initial capacity, see Fig. 7(b)), but it remains higher than the capacity of the electrodes based on the milled PW powders. For the 1h-milled, 3h-milled and 6h-milled PW-based electrodes, the specific capacity at the same rates decreases from 138 to 122 mAh·g^{-1} (89%), from 149.5 to 129 mAh·g^{-1} (86%), and from 151 to 126 mAh·g^{-1} (83%), respectively. When cycling at 5 and 10 C rates, the milled PW-based electrodes have a consistently higher capacity compared to the pristine PW-based electrode, whose capacity sharply decreases to 108 mAh·g^{-1} (72%) at 5 C and to ~ 77 mAh·g^{-1} (51%) at 10 C. The discharge capacity of the 1h-milled PW-based electrode is 115.5 mAh·g^{-1} (84%) at 5 C and 106.5 mAh·g^{-1} (77%) at 10 C; of the 3h-milled—122 mAh·g^{-1} (81%) and 112 mAh·g^{-1} (75%); of the 6h-milled—126 mAh·g^{-1} (83.5%) and 110 mAh·g^{-1} (73%), respectively. The electrode based on 1h-milled PW powder demonstrates the lowest specific capacity among the three milled PW-based electrodes. Charge–discharge curves of the electrodes prepared from pristine and milled PW powders as active materials at different cycling rates are shown in Fig. S6 in the ESM. The achieved capacities of the milled materials at 5 and 10 C rates exceed the previously reported capacities for the commercial material (see Table S6 in the ESM).

The cycling stability of electrodes based on pristine and milled PW powders was evaluated by repeating charge/discharge process for 300 cycles at 1 C rate in constant current–constant voltage (CC/CV) mode (Figs. 7(c)–7(e)) after cycling at different current densities (Figs. 7(a) and 7(b)). The first discharge specific capacity of the electrodes at 1 C rate (after the initialization cycles made at 0.1 C) was 129.7 mAh·g^{-1} for the pristine PW-based electrode, and 113.4, 141.4 and 144.8 mAh·g^{-1} for the electrodes based on 1h-milled, 3h-milled and 6h-milled powders, respectively. These capacity values are significantly lower than those obtained during the initial cycling at 1 C (Fig. 7(a)). As it was revealed in the previous investigations, this PW material exhibits a rapid capacity drop in the first few cycles even at 0.1 C cycling rate [8, 9], which could be associated with sodium inventory loss in the first cycles [43] or side reactions with the electrolyte leading to a high polarization.

The electrode prepared from the pristine PW shows the highest rate of capacity drop (dC/dN in Fig. 7(e)). Already after 50 cycles, its retained discharge specific capacity is only 68.3% (Coulombic efficiency is 99.4%), while for the electrodes based on milled powders, the retained capacities are at a level of 85%–90%. After 300 cycles, the electrode with 3h-milled active material has the best capacity of 73.7 mAh·g^{-1} (that is 52% of its initial value; the Coulombic efficiency stabilized at 99.3%) compared to 45.4 mAh·g^{-1} (35% of the initial capacity; the Coulombic efficiency is 99.6%) for the electrode based on the pristine PW; the 1h- and 6h-milled electrodes have specific capacities of about 66 mAh·g^{-1}. The intercalation of Na^+ into hexacyanoferrate structure is a two-stage process [35, 44]: The first stage is characterized by the redox reaction on Fe with high-spin configuration (HS-Fe) in FeN_6 octahedra during the intercalation of the first Na^+; the intercalation of the second Na^+ occurs at a redox reaction on Fe with low-spin configuration (LS-Fe) in the center of FeC_6 octahedra. This two-stage redox reaction mechanism is reflected in the two plateaus at a

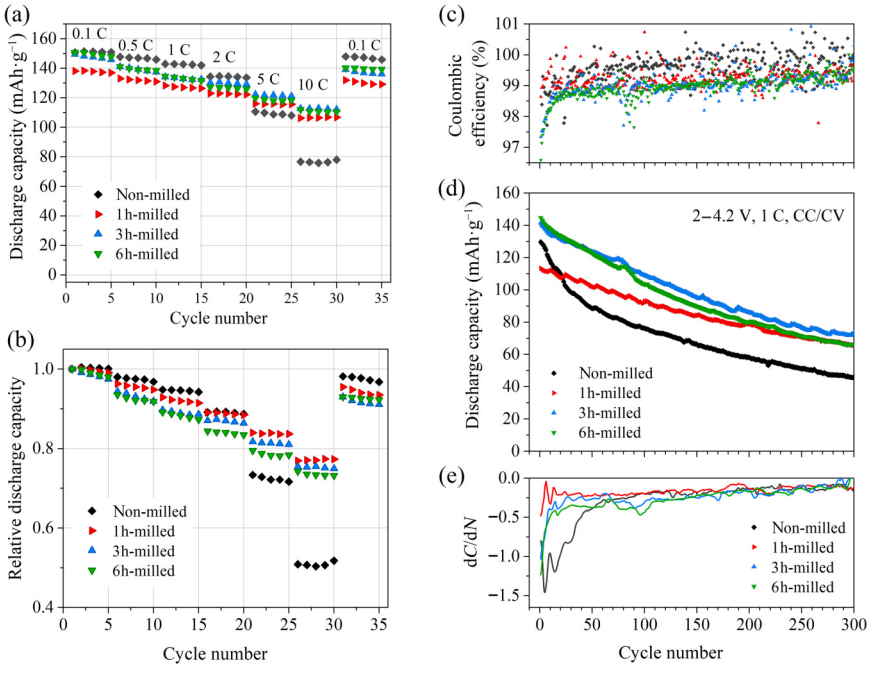

Figure 7 Rate performance of the electrodes based on the pristine and milled PW powders as an active material at rates from 0.1 to 10 C (1 C = 170 mAh·g^{-1}): (a) absolute discharge capacity and (b) discharge capacity relative to the first cycle at 0.1 C rate. Electrochemical performance of PW electrodes at 1 C rate within the 2.0 –4.2 V range: (c) Coulombic efficiency, (d) discharge capacity, and (e) rate of capacity decrease as functions of cycle number.

capacity–voltage curve [18, 35]: The low-voltage plateau at ~ 3.1 V corresponds to the redox couple HS-Fe$^{2+/3+}$ in the FeN_6 octahedra, and the high-voltage plateau at ~ 3.3 V corresponds to the redox couple LS-Fe$^{2+/3+}$ in the FeC_6 octahedra.

These plateaus are more evident as peaks in the plots of the derivative of capacity with respect to voltage (d*C*/d*V*). The plots for the cells with electrodes based on the pristine and 6h-milled PW powders at cycling rates of 0.1 and 5 C are given in Fig. 8 (for d*C*/d*V* plots of all the investigated electrodes, see Fig. S7 in the ESM). The peak at ~ 3.1 V is associated with the HS-Fe redox reaction (further "HS-Fe redox peak"); it is controlled by the ion-diffusion behavior [34]. For the non-milled material, the HS-Fe reduction/oxidation peak is at 3.12/3.00 V (3.14/2.96 V) with a hysteresis of 117 mV (180 mV), at 0.1 C (and 0.5 C) respectively. The HS-Fe redox peak is barely activated: At the 0.5 C rate, this peak is quite weak, and already at the 2 C rate, it is absent.

The HS-Fe redox peak on the d*C*/d*V* curve for the non-milled PW can be suppressed due to partial surface oxidation of the powder, which is the HS-Fe oxidation [9, 23]. This is confirmed by FTIR and XPS results (Figs. 2 and 3). The milling process increases the surface area of active material with non-oxidized HS-Fe, which produces an intensive HS-Fe redox peak in the d*C*/d*V* curves at cycling rates up to 5 C for all the milled materials (Fig. S7 in the ESM). Compared to non-milled electrode, for the milled PW-based electrodes, the HS-Fe redox peak shifts to lower voltages and has a noticeably smaller voltage hysteresis (80–83 mV at 0.1 C) during discharge (differences between HS-Fe redox peak positions at charge and discharge are given as insets in Fig. 8(c) and in Table S6 in the ESM), indicating the accelerated sodium diffusion in the milled materials compared to non-milled PW. Thus, mechanical milling may facilitate sodium diffusion due to reduction of ion diffusion paths in smaller particles of the active material.

The so-called pseudocapacitive effect (the charge storage of cations from faradaic processes occurring at the surface [45]), which is believed to control the high-voltage LS-Fe redox [34], apparently contributes to the stable cycling of the milled PW-based electrodes at high rates. Compared to the pristine PW-based electrode, the intensive LS-Fe redox peak with the small hysteresis shifts to lower voltages at 5 and 10 C on the d*C*/d*V* curves (Fig. 8(d)), while the peak positions are similar for all electrodes at lower cycling rates. Indeed, the electrodes based on the milled PW exhibit higher capacity at 5 and 10 C rates compared to the electrode based on the pristine active material (Fig. 7(a)).

The 3h-milled material has the lowest polarization among all milled samples (Table S7 in the ESM) and the best electrochemical stability during cycling (Fig. 7(d)). Apparently, the 3h-milled material has the optimal specific active surface, at which there is no excessive oxidation, as in the case of 6h-milled powder (see Fig. 3(g)) and water absorption due to short-term contact with the atmosphere and long-term storage in an argon-filled box.

To conclude, the data on the electrochemical performance of the active materials with different morphologies agree with our structural observations. When the milled material is electrochemically cycled in the 2–4.2 V range, the cubic phase does not transform into the R-phase, the appearance of which in diffraction patterns is observed only during discharge to voltages below 2 V (Fig. 6(b)). Thus, during electrochemical cycling, the milled material transforms between only two structural phases, cubic and dehydrated rhombohedral (Fig. 6). Reduction of the number of phase transitions should reduce the overall relaxation time during the transformations between phases, and hence, the sodium ion mobility in the material should increase, which explains the higher capacity of the electrode based on the milled PW powder at high rates of cycling (Fig. 7(a)). The milled materials show a higher capacity (Fig. 7(d)) after long-term cycling, likely due to the lower total number of phase transitions resulting in the accumulation of fewer structural deformations.

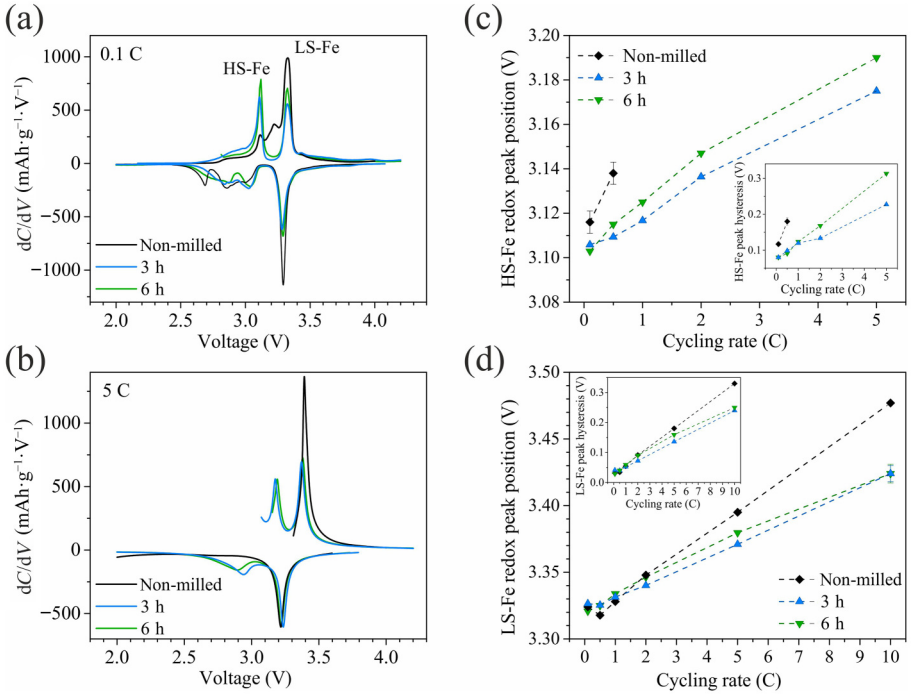

Figure 8 d*C*/d*V* curves for 70/15/15 electrodes during cycling at (a) 0.1 and (b) 5 C rates, and (c) HS-Fe and (d) LS-Fe peak positions at different cycling rates.

4 Conclusion

The study of the ball-milling effect on commercial Prussian white active material was conducted to investigate ways to improve its electrochemical properties as a cathode material for rechargeable sodium-ion batteries.

Mechanical milling of the pristine powder modifies its morphology, which leads to a change in the crystal structure, shifts the phase transition from the cubic phase into the dehydrated rhombohedral phase during heating to lower temperatures, and decreases a number of phase transformations in the material during electrochemical performance. The larger surface area of the PW particles produced during milling leads to more effective dehydration when the material is heated in vacuum and promotes the formation of the dehydrated rhombohedral phase. Particle fragmentation due to milling also compensates for the capacity loss resulting from the surface oxidation of the material after long-term storage. Due to these effects the grain-refined PW material with a particle size of several hundred nanometers demonstrates much better high-rate capacity (up to 112 mAh·g^{-1} at 10 C rate) and better long-term cycling stability compared to the pristine PW material. But prolonged ball-milling leads to formation of a large surface area of PW particles, which also may promote unnecessary surface oxidation of the material during storage. Further investigation of sodium migration mechanisms in the PW materials with different particle morphologies is planned to reveal additional correlation between their structure and electrochemical properties.

Electronic Supplementary Material: Supplementary material (XPS test data, Rietveld-fitted XRD patterns and results of Rietveld analysis, charge/discharge curves and d*C*/d*V* curves at different cycling rates, and comparison with literature results) is available in the online version of this article at https://doi.org/10.26599/NR.2025.94907280.

Data availability

All data needed to support the conclusions in the paper are presented in the manuscript and the Electronic Supplementary Material. Additional data related to this paper may be requested from the corresponding author upon request.

Acknowledgements

This work was financially supported by the Russian Science Foundation (No. 21-12-00261). Authors would like to express utmost gratitude to two anonymous reviewers who helped to improve the manuscript.

Declaration of competing interest

All the contributing authors report no conflict of interests in this work.

Author contribution statement

N. Y. S.: Conceptualization, funding acquisition, project administration, supervision, formal analysis, investigation, writing – original draft, review & editing. M. E. D.: Investigation, formal analysis, writing – original draft. R. N. V.: Formal analysis, investigation, writing – review & editing. S. V. S.: Investigation. E. A. K.: Investigation, formal analysis. A. S. S.: Investigation. E. V. A.: Investigation. S. G. P.: Investigation. R. N. M.: Investigation. N. A. K.: Investigation.

Use of AI statement

None.

References

[1] Yabuuchi, N.; Kubota, K.; Dahbi, M.; Komaba, S. Research

development on sodium-ion batteries. *Chem. Rev.* **2014**, *114*, 11636–11682.
[2] Hasa, I.; Mariyappan, S.; Saurel, D.; Adelhelm, P.; Koposov, A. Y.; Masquelier, C.; Croguennec, L.; Casas-Cabanas, M. Challenges of today for Na-based batteries of the future: From materials to cell metrics. *J. Power Sources* **2021**, *482*, 228872.
[3] Tapia-Ruiz, N.; Armstrong, A. R.; Alptekin, H.; Amores, M. A.; Au, H.; Barker, J.; Boston, R.; Brant, W. R.; Brittain, J. M.; Chen, Y. et al. 2021 roadmap for sodium-ion batteries. *J. Phys. Energy* **2021**, *3*, 031503.
[4] Liu, Y. A.; Liu, H. Q.; Zhang, R. Z.; Zhong, Y. J.; Wu, Z. G.; Wang, X. L.; Zhang, Z. Y. Recent progress of manganese-based Prussian blue analogue cathode materials for sodium-ion batteries. *Ionics* **2024**, *30*, 39–59.
[5] Lu, Y. H.; Wang, L.; Cheng, J. G.; Goodenough, J. B. Prussian blue: A new framework of electrode materials for sodium batteries. *Chem. Commun.* **2012**, *48*, 6544–6546.
[6] Peng, J.; Zhang, W.; Liu, Q. N.; Wang, J. Z.; Chou, S. L.; Liu, H. K.; Dou, S. X. Prussian Blue analogues for sodium-ion batteries: Past, present, and future. *Adv. Mater.* **2022**, *34*, 2108384.
[7] Yi, H. C.; Qin, R. Z.; Ding, S. X.; Wang, Y. T.; Li, S. N.; Zhao, Q. H.; Pan, F. Structure and properties of Prussian blue analogues in energy storage and conversion applications. *Adv. Funct. Mater.* **2021**, *31*, 2006970.
[8] Maddar, F. M.; Walker, D.; Chamberlain, T. W.; Compton, J.; Menon, A. S.; Copley, M.; Hasa, I. Understanding dehydration of Prussian white: From material to aqueous processed composite electrodes for sodium-ion battery application. *J. Mater. Chem. A* **2023**, *11*, 15778–15791.
[9] Samoylova, N. Y.; Bobrikov, I. A.; Razanau, I.; Sumnikov, S. V.; Vasin, R. N.; Korneeva, E. A.; Ponomareva, O. Y.; Novikau, U. Peculiarities of charge–discharge processes in Prussian white electrodes with different level of dehydration. *J. Alloys Compd.* **2024**, *983*, 173849.
[10] Yamada, A.; Chung, S. C.; Hinokuma, K. Optimized $LiFePO_4$ for lithium battery cathodes. *J. Electrochem. Soc.* **2001**, *148*, A224.
[11] Bobrikov, I. A.; Balagurov, A. M.; Hu, C. W.; Lee, C. H.; Chen, T. Y.; Sangaa, D.; Balagurov, D. A. Structural evolution in $LiFePO_4$-based battery materials: *In-situ* and *ex-situ* time-of-flight neutron diffraction study. *J. Power Sources* **2014**, *258*, 356–364.
[12] Ni, J. F.; Kawabe, Y.; Morishita, M.; Watada, M.; Sakai, T. Improved electrochemical activity of $LiMnPO_4$ by high-energy ball-milling. *J. Power Sources* **2011**, *196*, 8104–8109.
[13] Zhang, H.; Xu, Y. L.; Liu, D. Novel nanostructured $LiMn_2O_4$ microspheres for high power Li-ion batteries. *RSC Adv.* **2015**, *5*, 11091–11095.
[14] Lee, H. J.; Kim, D. Y.; Jeong, S. K. Effect of ball milling process on electrochemical properties of copper hexacyanoferrate active material for calcium-ion batteries. *Key Eng. Mater.* **2019**, *803*, 109–114.
[15] Peng, J.; Gao, Y.; Zhang, H.; Liu, Z. G.; Zhang, W.; Li, L.; Qiao, Y.; Yang, W. S.; Wang, J. Z.; Dou, S. X. et al. Ball milling solid-state synthesis of highly crystalline Prussian Blue analogue $Na_{2-x}MnFe(CN)_6$ cathodes for all-climate sodium-ion batteries. *Angew. Chem., Int. Ed.* **2022**, *61*, e202205867.
[16] He, S. L.; Zhao, J. M.; Rong, X. H.; Xu, C. L.; Zhang, Q. Q.; Shen, X.; Qi, X. G.; Li, Y. Q.; Li, X. Y.; Niu, Y. S. et al. Solvent-free mechanochemical synthesis of Na-rich Prussian white cathodes for high-performance Na-ion batteries. *J. Chem. Eng.* **2022**, *428*, 131083.
[17] Ma, N.; Ohtani, R.; Le, H. M.; Sørensen, S. S.; Ishikawa, R.; Kawata, S.; Bureekaew, S.; Kosasang, S.; Kawazoe, Y.; Ohara, K. et al. Exploration of glassy state in Prussian blue analogues. *Nat. Commun.* **2022**, *13*, 4023.
[18] Brant, W. R.; Mogensen, R.; Colbin, S.; Ojwang, D. O.; Schmid, S.; Häggström, L.; Ericsson, T.; Jaworski, A.; Pell, A. J.; Younesi, R. Selective control of composition in Prussian white for enhanced material properties. *Chem. Mater.* **2019**, *31*, 7203–7211.
[19] Wang, W. L.; Hu, Z.; Yan, Z. C.; Peng, J.; Chen, M. Z.; Lai, W. H.; Gu, Q. F.; Chou, S. L.; Liu, H. K. et al. Understanding rhombohedral iron hexacyanoferrate with three different sodium positions for high power and long stability sodium-ion battery. *Energy Stor. Mater.* **2020**, *30*, 42–51.
[20] Kraft, A. Some considerations on the structure, composition, and properties of Prussian blue: A contribution to the current discussion. *Ionics* **2021**, *27*, 2289–2305.
[21] Brunauer, S.; Emmett, P. H.; Teller, E. Adsorption of gases in multimolecular layers. *J. Am. Chem. Soc.* **1938**, *60*, 309–319.
[22] Lejeune, J.; Brubach, J. B.; Roy, P.; Bleuzen, A. Application of the infrared spectroscopy to the structural study of Prussian blue analogues. *C. R. Chim.* **2014**, *17*, 534–540.
[23] Ojwang, D. O.; Svensson, M.; Njel, C.; Mogensen, R.; Menon, A. S.; Ericsson, T.; Häggström, L.; Maibach, J.; Brant, W. R. Moisture-driven degradation pathways in Prussian white cathode material for sodium-ion batteries. *ACS Appl. Mater. Interfaces* **2021**, *13*, 10054–10063.
[24] Niwa, H.; Moriya, T.; Shibata, T.; Fukuzumi, Y.; Moritomo, Y. *In situ* IR spectroscopy during oxidation process of cobalt Prussian blue analogues. *Sci. Rep.* **2021**, *11*, 4119.
[25] Tang, D. J.; Wang, J. X.; Liu, X. A.; Tong, Z. F.; Ji, H. B.; Qu, H. Y. Low-Spin Fe Redox-Based Prussian Blue with excellent selective dual-band electrochromic modulation and energy-saving applications. *J. Colloid Interface Sci.* **2023**, *636*, 351–362.
[26] Luo, Y.; Peng, J. Y.; Yan, Y. W. Self-induced cobalt-derived hollow structure Prussian blue as a cathode for sodium-ion batteries. *RSC Adv.* **2021**, *11*, 31827–31833.
[27] Forment-Aliaga, A.; Weitz, R. T.; Sagar, A. S.; Lee, E. J. H.; Konuma, M.; Burghard, M.; Kern, K. Strong p-type doping of individual carbon nanotubes by Prussian blue functionalization. *Small* **2008**, *4*, 1671–1675.
[28] Lutterotti, L.; Matthies, S.; Wenk, H. R.; Schultz, A. S.; Richardson, J. W. Jr. Combined texture and structure analysis of deformed limestone from time-of-flight neutron diffraction spectra. *J. Appl. Phys.* **1997**, *81*, 594–600.
[29] Rietveld, H. M. A profile refinement method for nuclear and magnetic structures. *J. Appl. Cryst.* **1969**, *2*, 65–71.
[30] Wang, W. L.; Gang, Y.; Hu, Z.; Yan, Z. C.; Li, W. J.; Li, Y. C.; Gu, Q. F.; Wang, Z. X.; Chou, S. L.; Liu, H. K. et al. Reversible structural evolution of sodium-rich rhombohedral Prussian blue for sodium-ion Batteries. *Nat. Commun.* **2020**, *11*, 980.
[31] Rudola, A.; Du, K.; Balaya, P. Monoclinic sodium iron hexacyanoferrate cathode and non-flammable glyme-based electrolyte for inexpensive sodium-ion batteries. *J. Electrochem. Soc.* **2017**, *164*, A1098–A1109.
[32] Balagurov, A. M.; Bobrikov, I. A.; Bokuchava, G. D.; Vasin, R. N.; Gusev, A. I.; Kurlov, A. S.; Leoni, M. High-resolution neutron diffraction study of microstructural changes in nanocrystalline ball-milled niobium carbide $NbC_{0.93}$. *Mater. Charact.* **2015**, *109*, 173–180.
[33] Patnaik, S. G.; Escher, I.; Ferrero, G. A.; Adelhelm, P. Electrochemical study of Prussian white cathodes with glymes-pathway to graphite-based sodium-ion battery full cells. *Batteries Supercaps* **2022**, *5*, e202200043.
[34] Sun, J. G.; Ye, H. L.; Oh, J. A. S.; Plewa, A.; Sun, Y.; Wu, T.; Sun, Q. M.; Zeng, K. Y.; Lu, L. Elevating the discharge plateau of prussian blue analogs through low-spin Fe redox induced intercalation pseudocapacitance. *Energy Stor. Mater.* **2021**, *43*, 182–189.
[35] Wang, L.; Song, J.; Qiao, R. M.; Wray, L. A.; Hossain, M. A.; Chuang, Y. D.; Yang, W. L.; Lu, Y. H.; Evans, D.; Lee, J. J. et al. Rhombohedral Prussian white as cathode for rechargeable sodium-ion batteries. *J. Am. Chem. Soc.* **2015**, *137*, 2548–2554.
[36] Piernas-Muñoz, M. J.; Castillo-Martínez, E.; Bondarchuk, O.;

Armand, M.; Rojo, T. Higher voltage plateau cubic Prussian white for Na-ion batteries. *J. Power Sources* **2016**, *324*, 766–773.

[37] Tang, W.; Xie, Y. Y.; Peng, F. W.; Yang, Y.; Feng, F.; Liao, X. Z.; He, Y. S.; Ma, Z. F.; Chen, Z. H.; Ren, Y. Electrochemical performance of $NaFeFe(CN)_6$ prepared by solid reaction for sodium ion batteries. *J. Electrochem. Soc.* **2018**, *165*, A3910–A3917.

[38] You, Y.; Wu, X. L.; Yin, Y. X.; Guo, Y. G. High-quality Prussian blue crystals as superior cathode materials for room-temperature sodium-ion batteries. *Energy Environ. Sci.* **2014**, *7*, 1643–1647.

[39] Xi, Y. M.; Lu, Y. C. Facile synthesis and cycling performance maintenance of iron hexacyanoferrate cathode for sodium-ion battery. *J. Power Sources* **2021**, *513*, 230554.

[40] Nielsen, I.; Dzodan, D.; Ojwang, D. O.; Henry, P. F.; Ulander, A.; Ek, G.; Häggström, L.; Ericsson, T.; Boström, H. L. B.; Brant, W. R. Water driven phase transitions in Prussian white cathode materials. *J. Phys. Energy* **2022**, *4*, 044012.

[41] Wang, W. L.; Gang, Y.; Peng, J.; Hu, Z.; Yan, Z. C.; Lai, W. H.; Zhu, Y. F.; Appadoo, D.; Ye, M.; Cao, Y. L. et al. Effect of eliminating water in Prussian blue cathode for sodium-ion batteries. *Adv. Funct. Mater.* **2022**, *32*, 2111727.

[42] Ponomareva, O. Y.; Sumnikov, S. V.; Vasin, R. N.; Korneeva, E. A.; Samoylova, N. Y. Phase transformations in Na-rich Prussian white cathode materials with different morphology. *Phys. Part. Nuclei Lett.* **2024**, *21*, 764–767.

[43] Nielsen, I.; Hall, C. A.; Mattsson, A. M.; Younesi, R.; Buckel, A.; Ek, G.; Brant, W. R. Unravelling the origin of capacity fade in Prussian white hard carbon full cells through *operando* X-ray diffraction. *J. Mater. Chem. A* **2024**, *12*, 17413–17421.

[44] Ling, C.; Chen, J. J.; Mizuno, F. First-principles study of alkali and alkaline earth ion intercalation in iron hexacyanoferrate: The important role of ionic radius. *J. Phys. Chem. C* **2013**, *117*, 21158–21165.

[45] Brezesinski, T.; Wang, J.; Polleux, J.; Dunn, B.; Tolbert, S. H. Templated nanocrystal-based porous TiO_2 films for next-generation electrochemical capacitors. *J. Am. Chem. Soc.* **2009**, *131*, 1802–1809.